Available online at www.sciencedirect.com
SCIENCE DIRECT
International Journal of Heat and Mass Transfer 49 (2006) 2239–2253
International Journal of HEAT and MASS TRANSFER
www.elsevier.com/locate/ijhmt

Heat and mass transfer in tubular ceramic membranes for membrane reactors

A. Hussain [a], A. Seidel-Morgenstern [a,b], E. Tsotsas [a,*]

[a] Institute of Process Engineering, Otto-von-Guericke-University, 39106 Magdeburg, Germany
[b] Max-Planck-Institut für Dynamik komplexer technischer Systeme Magdeburg, Germany

Received 27 April 2005; received in revised form 21 October 2005
Available online 13 March 2006

Abstract

Six different types of experiments are used in order to identify and validate the heat and mass transfer parameters of a tubular membrane. The respective configuration is similar to that of a membrane reactor, though without particulate catalyst or catalytic coating. The membrane is made of various layers of α- and γ-Al_2O_3 and has dimensions (inner diameter of 21 mm) close to those relevant for practical applications. Mass transfer parameters of every single layer are derived separately by means of dusty gas model, pointing out unexpected effects of asymmetry. Experiments of steady-state heat transfer, dynamic heat transfer, and combined heat and mass transfer are introduced, thermal influences on mass transfer are discussed. Four of the six conducted types of experiments are free of fitting, providing a successful test of accuracy and consistency of the identified transport parameters, and a basis for a reliable simulation of membrane reactors.
© 2006 Elsevier Ltd. All rights reserved.

Keywords: Ceramic membranes; Membrane reactor; Heat transfer; Gas permeation; Gas diffusion; Dusty gas model

1. Introduction

Membrane technology offers a great potential to achieve higher conversion or better selectivity in chemical reactors by selective removal of products or controlled, spatially distributed supply of reactants [1,2]. In membrane reactors for gas–solid catalytic reactions (dehydrogenations [3–5], partial oxidations [6]) either particulate catalyst is placed in the interior of the tubular membrane, or the membrane itself is impregnated or coated with catalyst. In both cases, the membrane must be able to withstand the necessary elevated temperatures and chemical environment. Polymer membranes fail to this respect, so that inorganic membranes must be used [7]. Such membranes can be dense (e.g., ion conductors) or porous, and may consist of only one or of many layers. Multilayer asymmetric membranes usually consist of permselective material as a thin film on one or a series of porous supports, which provide the required mechanical stability without dramatically reducing the total transmembrane flux [8].

With increasing technical applications, the modelling of membrane reactors has attracted interest over the last decade. Most studies focus on a particular membrane reactor system, aiming to quantify its performance in terms of attainable yield and selectivity (see, among others [9–14]). Comprehensive reviews develop and treat general mathematical models for membrane reactors, providing solutions for special cases [1,7]. While isothermal conditions are often assumed [11–13], thermal effects are recognized as an important issue in some membrane reactor models [9,10]. The thermal conductivity of membranes is usually taken as constant, assuming negligible temperature gradients in the membrane [12,14].

Since membranes are the primary component of membrane reactors, every reactor model must describe transport

* Corresponding author. Address: Evangelos Tsotsas, P.O.B. 4120, Magdeburg D-39016, Germany. Tel.: +49 391 67 18782; fax: +49 391 67 11160.
E-mail address: evangelos.tsotsas@vst.uni-magdeburg.de (E. Tsotsas).

0017-9310/$ - see front matter © 2006 Elsevier Ltd. All rights reserved.
doi:10.1016/j.ijheatmasstransfer.2005.12.006

Nomenclature

A	area [m^2]
B_0	permeability constant in dusty gas model [m^2]
c	heat capacity [J/kg K]
$\tilde{c}$	molar heat capacity [J/mol K]
d	diameter [m]
D_{ax}	axial dispersion coefficient [m^2/s]
D	diffusion coefficient [m^2/s]
F_0	ratio of effective to molecular diffusion coefficient [–]
F	cross-sectional area [m^2]
K_0	Knudsen coefficient in dusty gas model [m]
L	length [m]
$\widetilde{M}$	molar mass [kg/mol]
n	molar density [mol/m^3]
$\dot{n}$	molar flux [mol/m^2 s]
$\dot{N}$	molar flow rate [mol/s]
Nu	Nusselt number [–]
P	absolute pressure [Pa]
Pr	Prandtl number [–]
$\dot{q}$	heat flux [W/m^2]
$\dot{Q}$	heat flow rate [W]
r	radial coordinate [m]
$\tilde{r}$	mean membrane radius [m]
$\widetilde{R}$	gas constant [J/mol K]
Sc	Schmidt number [–]
Sh	Sherwood number [–]
t	time [s]
T	temperature [K, °C]
u	flow velocity [m/s]
V	volume [m^3]
$\tilde{x}$	mole fraction [–]
z	axial coordinate [m]

Greek symbols

α	heat transfer coefficient [W/m^2K]
β	mass transfer coefficient [m/s]
ε	porosity [–]
η	viscosity [Pa s]
κ	thermal diffusivity [m^2/s]
λ	thermal conductivity [W/mK]
Λ_{ax}	axial thermal dispersion coefficient [W/mK]
ρ	density [kg/m^3]
τ	tortuosity [–]

Indices

av	average
e	effective
g	gas
in	inlet
i	inner, tube side of the membrane
j, k	species in the mixture
K	Knudsen
m	membrane
o	outer, annulus side of the membrane
out	outlet
p	pore
P	at constant pressure
shell	shell

kinetics through the membrane accounting for its complicated structure. Several researchers have contributed to the characterization of porous inorganic membranes by identifying the mass transfer parameters of the membrane during the recent years [15,16]. In [17–19] single layer glass and metallic membranes are investigated by experiments of steady-state gas permeation, isobaric diffusion and transient diffusion in order to obtain the parameters of the dusty gas model (DGM). Surface diffusion is additionally taken into consideration in [18]. The approach is extended to two layer ceramic membranes in [20]. Finally, multilayer porous ceramic membranes are characterized on the basis of steady-state permeation experiments in [21,22]. Measurements of thermal properties are not available.

The present work focuses on the independent and separate determination of all data about heat and mass transfer through multilayer tubular ceramic membranes (porous aluminium oxide) that is necessary for modelling and optimization of membrane reactors. Though we do not yet consider chemical reaction, the partial oxidation of ethane to ethylene or butane to maleic acid anhydride is the background of the investigation. Consequently, the controlled dosage of oxygen is the purpose of the membrane. We take over the methods described in [17–22] and expand them to a comprehensive experimental matrix consisting of six different experiments. Some of these experiments are steady state, some others dynamic; some are used to identify the transport parameters of the membrane, some others to validate them by predicting the measured results without any fitting. For the first time in literature, heat transfer as well as combined heat and mass transfer are integrated to this analysis, giving insight on how mass transfer is influenced by temperature distribution and heat transfer through porous membranes. Some aspects of multilayer gas permeation that have not been discussed before are pointed out. Furthermore, the membranes used in this work are comparatively larger than the membranes used in earlier investigations [19–21], realistically corresponding to membrane dimensions for application on industrial scale.

The paper is organized by first giving a short overview of the six conducted experiments. Then the models used for heat and mass transfer are described in general form. Some more details are given on the experimental set-up and materials. Subsequently, the conducted experiments and their evaluation are discussed one-by-one, starting with

heat transfer, continuing with mass transfer and ending with coupled heat and mass transfer.

2. Experimental matrix

The six types of experiments conducted in the present work are

- steady-state heat transfer (identification),
- transient heat transfer (validation),
- single gas permeation (identification),
- steady-state isobaric diffusion (validation),
- transient diffusion (validation),
- steady-state heat and mass transfer (validation).

Fig. 1 recapitulates the principle of every experiment, indicating state variables and operating parameters that are used in order to derive the heat and mass transport parameters of the membrane, or measured to the purpose of validation by comparison with model predictions. It will be pointed out later that the single gas permeation experiment has also validation components. Notice that the sketches realistically show the reactor geometry, consisting of a shell-side (annulus, index "o") and a tube-side (index "i") space. The latter will be filled with particulate catalyst in reactor operation, oxygen will be supplied from the annulus.

3. Heat transfer model

The model equations for thermal experiments with and without mass transfer consider in the general case all important heat transfer modes in and along the membrane except radiation. Boundary and initial conditions are also

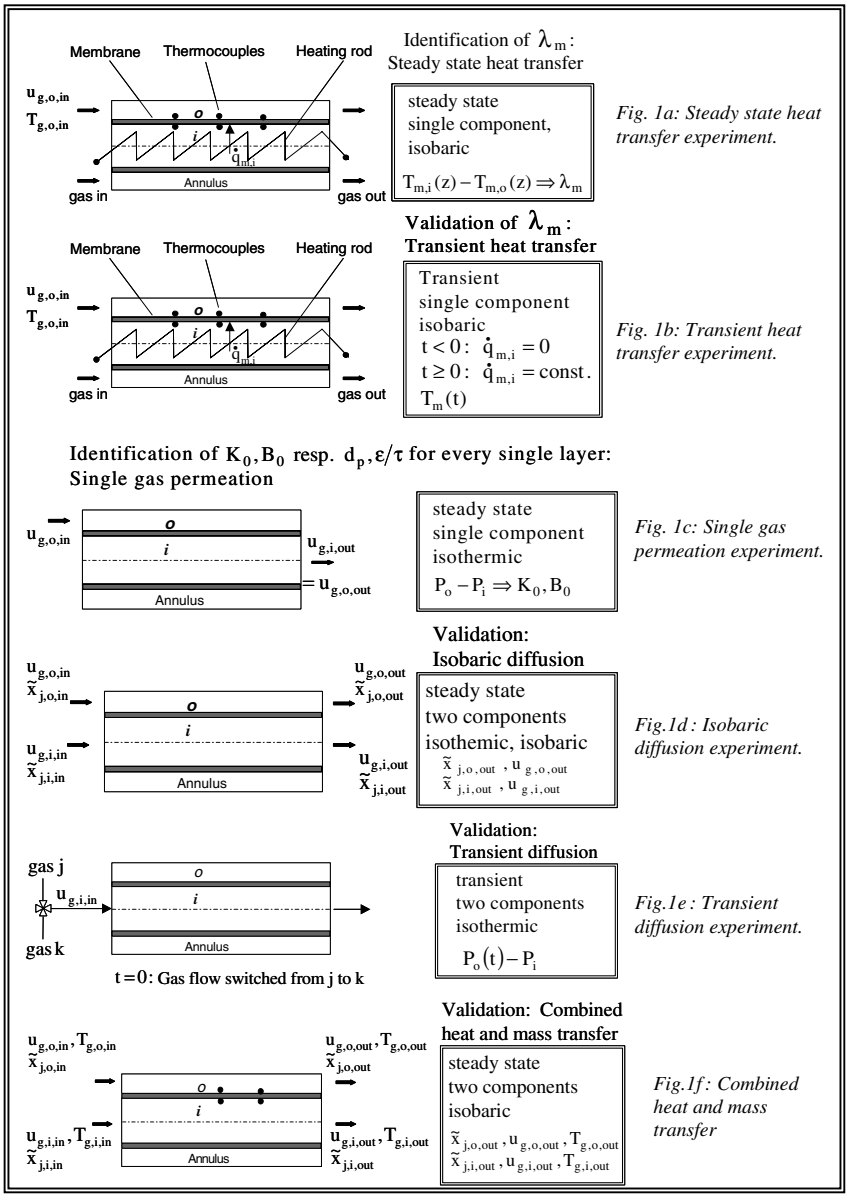

Fig. 1. Experimental matrix for the identification and validation of transport parameters.

expressed here in a general way. During the evaluation of experiments, some of them will be discarded, modified or specified.

The energy balance for the membrane, i.e., for the space

$$r_{m,i} < r < r_{m,o}, \quad 0 < z < L$$

is formulated in two dimensions and cylindrical coordinates to

$$\rho_m \frac{\partial(c_m T_m)}{\partial t} = \frac{1}{r}\frac{\partial}{\partial r}\left(r\lambda_m \frac{\partial T_m}{\partial r}\right) + \frac{\partial}{\partial r}\left(\sum_j \dot{n}_j \tilde{c}_{p,g,j} T_m\right) + \frac{\partial}{\partial z}\left(\lambda_m \frac{\partial T_m}{\partial z}\right). \quad (1)$$

The temporal change in gas temperature has been ignored and a local thermal equilibrium has been assumed between gas and solid in the membrane. The respective boundary and initial conditions are

$$r = r_{m,i}: \quad -\lambda_m \frac{\partial T_m}{\partial r} = \dot{q}_{m,i}, \quad (2a)$$

$$r = r_{m,o}: \quad -\lambda_m \frac{\partial T_m}{\partial r} = \dot{q}_{m,o}, \quad (2b)$$

where

$$\dot{q}_{m,i} = \alpha_{g,i}(T_{g,i} - T_{m,i}), \quad (2c)$$

$$\dot{q}_{m,o} = \alpha_{g,o}(T_{m,o} - T_{g,o}), \quad (2d)$$

$$z = 0: \quad \frac{\partial T_m}{\partial z} = 0, \qquad z = L: \quad \frac{\partial T_m}{\partial z} = 0, \quad (3a, b)$$

$$t = 0: \quad T_m = T_{m,0}. \quad (4)$$

As Eq. (1) shows, the dependence of the thermal conductivity of the membrane, λ_m, upon temperature is accounted for. Eqs. (2a), (2c) and (2b), (2d) define boundary conditions of the third kind at the inner and outer side of the membrane, respectively. Eqs. (3) assume both membrane ends to be insulated, while Eq. (4) sets the initial condition in the transient heat transfer case. The energy balance for the gas flowing in the annulus has been formulated in one-dimensional way to

$$\Lambda_{ax,o}\frac{d^2 T_{g,o}}{dz^2} - \frac{d\left(u_{g,o} n_{g,o} \tilde{c}^{av}_{p,g,o} T_{g,o}\right)}{dz} + \left\{\dot{q}_{m,o} + \sum_j \left(\dot{n}_{j,m,o} \tilde{c}_{p,g,j} T_{m,o}\right)\right\}\frac{2\pi r_{m,o}}{F_o} = 0. \quad (5)$$

By analogy, the energy balance of gas flowing in the tube can be written as

$$\Lambda_{ax,i}\frac{d^2 T_{g,i}}{dz^2} - \frac{d\left(u_{g,i} n_{g,i} \tilde{c}^{av}_{p,g,i} T_{g,i}\right)}{dz} - \left\{\dot{q}_{m,i} + \sum_j \left(\dot{n}_{j,m,i} \tilde{c}_{p,g,j} T_{m,i}\right)\right\}\frac{2\pi r_{m,i}}{F_i} = 0. \quad (6)$$

The required boundary conditions at the inlet and outlet of the annulus and tube are taken after Danckwerts,

$$z = 0: \quad u_{g,o} n_{g,o} \tilde{c}^{av}_{p,g,o}(T_{g,o,in} - T_{g,o}) + \Lambda_{ax,o}\frac{dT_{g,o}}{dz} = 0, \quad (7a)$$

$$u_{g,i} n_{g,i} \tilde{c}^{av}_{p,g,i}(T_{g,i,in} - T_{g,i}) + \Lambda_{ax,i}\frac{dT_{g,i}}{dz} = 0, \quad (7b)$$

$$z = L: \quad \frac{dT_{g,o}}{dz} = 0, \quad \frac{dT_{g,i}}{dz} = 0. \quad (8a, b)$$

It, furthermore, holds

$$z = 0: \quad u_{g,o} = u_{g,o,in}, \quad u_{g,i} = u_{g,i,in}. \quad (9a, b)$$

Molar gas density and average specific heat capacity are calculated according to

$$n_g = \frac{P}{\tilde{R} T_g}, \quad \tilde{c}^{av}_{p,g} = \sum_j \tilde{c}_{p,g,j} \tilde{x}_j \quad (10)$$

and may change with changing temperature and composition along the reactor, which must also be considered in the inlet boundary conditions.

The described model equations and boundary conditions are modified to solve every specific case of heat transfer from the mentioned experimental matrix.

4. Mass transfer model

In the present work the Dusty Gas Model (DGM) has been used to describe mass transfer through the porous membrane. The model is based on the idea of considering the solid phase as large molecules (''dust'') in a multicomponent gas mixture in order to capture the complex combination of viscous flow, Knudsen diffusion and molecular diffusion in porous media [15–21]. Viscous flow is bulk, non-separating flow caused by total pressure gradients, while in the Knudsen regime the transport is controlled by molecule–wall interactions, so that the molecules travel independently from each other. In contrary, molecule–molecule interactions define the molecular (ordinary, continuum) diffusion.

In its general form, the dusty gas model for species j in a mixture of N components is expressed by the relationship

$$\sum_{k=1,k\neq j}^{N} \frac{\tilde{x}_k \dot{n}_j - \tilde{x}_j \dot{n}_k}{D^e_{jk}} + \frac{\dot{n}_j}{D_{K,j}} = -\frac{P}{\tilde{R}T}\nabla \tilde{x}_j - \frac{\tilde{x}_j}{\tilde{R}T}\left(1 + \frac{B_0}{\eta_j D_{K,j}}\overline{P}\right)\nabla P, \quad (11)$$

where $j = 1$–N. The driving forces are included in the right-hand part of Eq. (11) in terms of total pressure and molar fraction (partial pressure) gradients, while the resulting fluxes, $\dot{n}_j$, appear at the left-hand side of the equation.

The mass balance for gas flowing in the annulus has been formulated in one-dimensional way to

$$D_{ax,o}\frac{d^2 \tilde{x}_{j,o}}{dz^2} - \frac{d}{dz}\left(u_{g,o}\frac{n_{g,o}}{n_{g,o,in}}\tilde{x}_{j,o}\right) + \frac{2\pi r_{m,o}}{F_o n_{g,o,in}}\dot{n}_{j,m,o} = 0. \quad (12)$$

In the tube it holds

$$D_{\mathrm{ax,i}}\frac{\mathrm{d}^2\tilde{x}_{j,\mathrm{i}}}{\mathrm{d}z^2}-\frac{\mathrm{d}}{\mathrm{d}z}\left(u_{\mathrm{g,i}}\frac{n_{\mathrm{g,i}}}{n_{\mathrm{g,i,in}}}\tilde{x}_{j,\mathrm{i}}\right)-\frac{2\pi r_{\mathrm{m,i}}}{F_{\mathrm{i}}n_{\mathrm{g,i,in}}}\dot{n}_{j,\mathrm{m,i}}=0. \tag{13}$$

The boundary conditions at the inlet and outlet of annulus and tube are taken again after Danckwerts,

$$z=0:\quad u_{\mathrm{g,o}}\left(\tilde{x}_{j,\mathrm{o,in}}-\tilde{x}_{j,\mathrm{o}}\right)+D_{\mathrm{ax,o}}\frac{\mathrm{d}\tilde{x}_{j,\mathrm{o}}}{\mathrm{d}z}=0, \tag{14}$$

$$u_{\mathrm{g,i}}\left(\tilde{x}_{j,\mathrm{i,in}}-\tilde{x}_{j,\mathrm{i}}\right)+D_{\mathrm{ax,i}}\frac{\mathrm{d}\tilde{x}_{j,\mathrm{i}}}{\mathrm{d}z}=0, \tag{15}$$

$$z=L:\qquad \frac{\mathrm{d}\tilde{x}_{j,\mathrm{o}}}{\mathrm{d}z}=0,\quad \frac{\mathrm{d}\tilde{x}_{j,\mathrm{i}}}{\mathrm{d}z}=0, \tag{16a, b}$$

whereby Eqs. (9) still apply at the inlet. At the membrane–gas interfaces it is

$$\dot{n}_{j,\mathrm{m,o}}=\beta_{\mathrm{g,o}}n_{\mathrm{g,m,o}}\left(\tilde{x}_{j,\mathrm{m,o}}-\tilde{x}_{j,\mathrm{o}}\right), \tag{17a}$$

$$\dot{n}_{j,\mathrm{m,i}}=\beta_{\mathrm{g,i}}n_{\mathrm{g,m,i}}\left(\tilde{x}_{j,\mathrm{i}}-\tilde{x}_{j,\mathrm{m,i}}\right). \tag{17b}$$

The relationship between flow rates and fluxes can be written as

$$\dot{n}_{j,\mathrm{m,o}}=\dot{N}_j/(2\pi r_{\mathrm{m,o}}L), \tag{18a}$$

$$\dot{n}_{j,\mathrm{m,i}}=\dot{N}_j/(2\pi r_{\mathrm{m,i}}L). \tag{18b}$$

The coefficients for Knudsen and for molecular diffusion can be expressed in the form

$$D_{\mathrm{K},j}=\frac{4}{3}K_0\sqrt{\frac{8\widetilde{R}T}{\pi\widetilde{M}_j}} \tag{19}$$

and

$$D^{\mathrm{e}}_{jk}=F_0D_{jk}, \tag{20}$$

respectively. Consequently the model has three parameters, B_0, K_0 and F_0, for capturing the influence of the structure of any specific porous body on viscous flow, bulk diffusion and molecular diffusion.

With the additional assumption of tortuous, monodispersed capillaries, which are neither interconnected, nor change their cross-sectional area with their length, the mentioned three parameters of the dusty gas model can be expressed as

$$B_0=F_0\frac{d_{\mathrm{p}}^2}{32}, \tag{21}$$

$$K_0=F_0\frac{d_{\mathrm{p}}}{4}, \tag{22}$$

$$F_0=\frac{\varepsilon}{\tau}, \tag{23}$$

and are, thus, reduced to a set of only two morphological parameters, namely

$$d_{\mathrm{p}}=\frac{8B_0}{K_0}, \tag{24}$$

the diameter of the assumed capillaries, and

$$\frac{\varepsilon}{\tau}=\frac{(K_0)^2}{2B_0} \tag{25}$$

with ε the porosity and τ the tortuosity of the body. It should be stressed that d_{p} and ε/τ are, in spite of their morphological reference, still more or less strongly lumped model parameters, which do not necessarily and exactly correspond to, e.g., the average pore diameter that might be determined by image analysis. A priori prediction of B_0, K_0 and F_0 would pre-suppose the rigorous transition from microscopical structure to macroscopical properties. Though considerable efforts are invested in this direction, the problem of reliable micro–macro transition is still not solved.

Binary diffusion coefficients, D_{jk}, have been calculated in the present work by means of the Chapman–Enskog equation [23].

5. Experimental set-up, materials

The experimental set-up is illustrated in Fig. 2. Various valves and mass flow controllers enable to accurately dose gases at the tube and/or annulus side of the reactor, where the tubular membranes to be investigated are placed. The gas flow rates are measured at both outlets by various instruments, depending on their absolute value. Additionally, a thermal conductivity GC sensor measures the gas composition. Not only absolute pressures are measured in the tube and annulus, but the respective pressure difference is also determined separately, in order to increase the accuracy in the evaluation of non-isobaric experiments. Isobaric conditions are attained by fine-adjustment of the needle valves at both gas outlets, and are monitored with the mentioned differential pressure gauge. As different mass transport mechanisms are temperature dependent, it is necessary to conduct the experiments at various temperature levels, which is achieved by placing the reactor in a controllable oven. Additional gas pre-heaters, post-coolers and insulations facilitate specific modes of operation. Furthermore, an electrical heater can be placed in the tube. The capacity of this heater is measured accurately. Apart from gas inlet and outlet temperatures, temperatures at the inner and outer membrane wall are also determined in some experiments. From various techniques that have been checked to this purpose the most efficient was to fix miniature thermocouples (type K, outer diameter: 0.5 mm) with a ceramic glue (Fortafix, Fa. Detakta, Norderstedt, Germany), which is especially suitable for metal–ceramic fixations and stable up to 1000 °C. Trendows software enables the automatic acquisition of experimental data. In the total, the experimental set-up can be seen as a generalised Wicke–Kallenbach cell for annular samples—generalised in the sense of enabling much more modes of operation than the classical configuration.

Appropriate sealing has been a crucial topic of experimental work. After trying out conventional O-rings and slightly conical graphite rings, the use of ceramic glue has been found to be optimal. A sketch of the measuring cell with this type of sealing is depicted in Fig. 3. Tightness to the environment as well as between the compartments

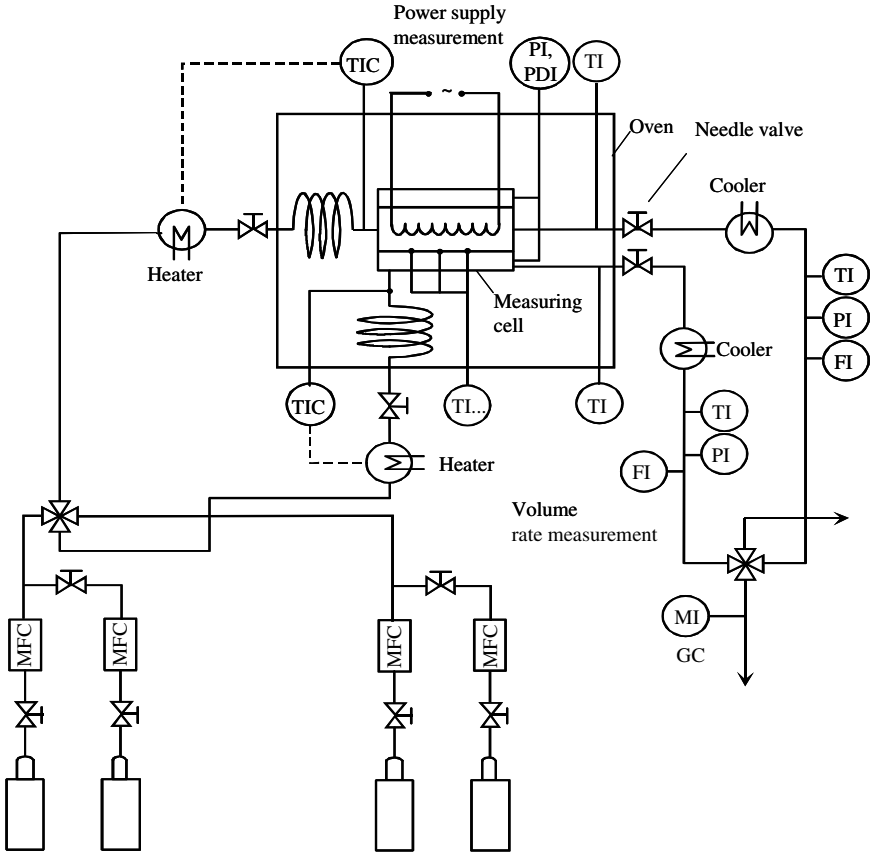

Fig. 2. Flow diagram of the experimental set-up (MFC: mass flow controller).

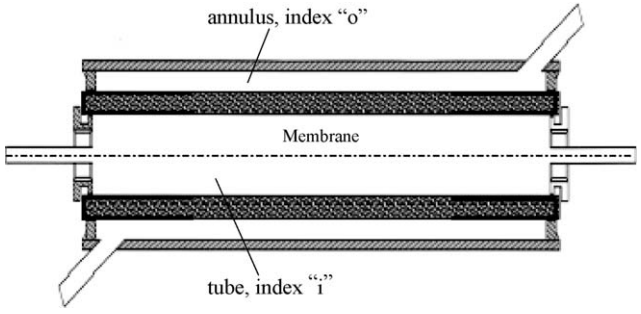

Fig. 3. Sketch of the measuring cell sealed with ceramic glue.

of the cell has been checked frequently during the measurements by a helium leakage detector and by pressure measurements.

All experiments reported here have been carried out with tubular ceramic membranes produced by the Inocermic GmbH, Hermsdorf, Germany, with a length of $L = 250$ mm, inner radius of $r_{m,i} = 10.5$ mm and outer radius of $r_{m,o} = 16$ mm (approximately). Both membrane ends were sealed by glass coating to a distance of 65 mm, so that the length effective for mass transfer was $L = 120$ mm. The composite consisted of a support, two further α-Al_2O_3 layers and the separation layer of γ-Al_2O_3 at the inner side. Respective layer thicknesses according to the producer are summarized in Table 1, along with nominal, coarsely approximate pore diameters. Every precursor of the asymmetric composite (only support, support plus one additional layer, support plus two additional layers) was available. Mass transfer experiments have also been conducted with a small membrane ($r_{m,i} = 3.5$ mm), revealing good agreement with previous comparable results by Thomas [22], will, however, not be presented here.

Table 1
Producer information and identified mass transfer parameters of membranes

Layer	Composition	Nominal d_p [m]	Thickness [m]	K_0 [m]	B_0 [m^2]	d_p [m]	ε/τ [–]
Support	α-Al_2O_3	3.0×10^{-6}	5.5×10^{-3}	8.16×10^{-8}	2.96×10^{-14}	2.90×10^{-6}	0.112
First layer	α-Al_2O_3	1.0×10^{-6}	25×10^{-6}	7.99×10^{-8}	2.73×10^{-14}	2.73×10^{-6}	0.124
Second layer	α-Al_2O_3	60×10^{-9}	25×10^{-6}	2.98×10^{-9}	2.85×10^{-17}	76.5×10^{-9}	0.156
Third layer	γ-Al_2O_3	10×10^{-9}	2×10^{-6}	2.03×10^{-9}	7.47×10^{-18}	29.4×10^{-9}	0.277

6. Heat transfer experiments

In heat transfer experiments an electrical heater is placed in the tube to supply a constant heat flux at the inner side of the membrane (Fig. 1a). There is no gas flow in the tube, gas, in our case air, flows only through the annulus. The membrane investigated in heat transfer experiments is the support of the composite after Table 1, which dominates the thermal behaviour. Thermocouples (Fig. 1a) are placed at axial positions of approximately $z = 70$, 125, 180 mm to measure the membrane inner and outer temperatures. The exact axial position of every thermocouple is determined after fixing. Transient thermal experiments have been conducted in similar manner by monitoring the change in membrane temperature after switching on the electrical heater at $t = 0$, see Fig. 1b.

6.1. Identification experiment: steady-state heat transfer

Steady-state heat transfer experiments after Fig. 1a have been used for the determination of the thermal conductivity of the membrane, λ_m. In these experiments the inlet flow velocity of the gas in the annulus ranged from $u_{g,o,in} = 0.15$–0.58 m/s and the imposed heat flux from $\dot{q}_{m,i} = 750\ \mathrm{W/m^2}$ to $5000\ \mathrm{W/m^2}$, corresponding to heat flow rates of $\dot{Q}_i = 15$–100 W. Axial temperature gradients of up to 9.4 K/cm and radial temperature gradients of up to 26.9 K/cm were found in the membrane.

Identification has not been conducted by the complete set of equations from Section 3. Instead, the well known reduction of Eq. (1) to one (the radial) dimension for the steady state with boundary conditions of the first kind at both $r_{m,i}$ and $r_{m,o}$ has been used. This pre-supposes negligible axial conduction, and is only justified because we measure locally temperature differences between the inner and the outer side of the membrane. As there is no gas flow in the tube, the enthalpy flux term of Eq. (1) can be dropped. Apart from simplicity, this approach has the advantage of not requiring knowledge of the heat transfer coefficient to the annulus gas, $\alpha_{g,o}$. From every measured local temperature difference one value of the thermal conductivity of the membrane is derived and attributed to the arithmetic average of the respective two temperatures. The results have been correlated empirically with the relationship

$$\lambda_m = -5.7372 \ln(T_m) + 38.853, \tag{26}$$

which is depicted as the bold solid lines in Fig. 4. Broken lines indicate maximal deviations, defining the area where all derived thermal conductivities lie.

The findings reveal that the thermal conductivity of the membrane decreases significantly with increasing temperature. This behaviour can be explained by defect scattering during phonon transport. According to Debbie, the thermal conductivity of solids can be derived by analogy to kinetic gas theory as $\lambda = c_V v \Lambda/3$, where c_V is the specific heat, v is the average velocity of the phonon and Λ is the phonon mean free path [24]. The latter can be expressed in the form $\Lambda = a/(\alpha\gamma T)$ (a: inter-atomic distance, α: thermal expansion coefficient, γ: Gruneisen parameter) [25]. Lawson transformed the equation to $\lambda = (aK^{3/2})/(3\gamma^2\rho^{1/2}T)$ by assuming that average phonon velocity is the same as the dilatational wave velocity (K: bulk modulus, ρ: density of the crystal structure) [26]. The proposed inversely proportional dependence of thermal conductivity on thermodynamic temperature is verified by the experimental data, though the value of intercept would be different than zero (Fig. 4, right-hand side plot). Respective correlations are possible, with similar accuracy as Eq. (26).

To obtain a more comprehensive picture of the temperature field in the membrane (Fig. 5) the complete equations of Section 3 are solved numerically for the steady state, though without transmembrane enthalpy flux, tube-side convection, and axial dispersion of annulus flow. These simulations are two-dimensional in respect to the membrane and require, in contrary to the conducted

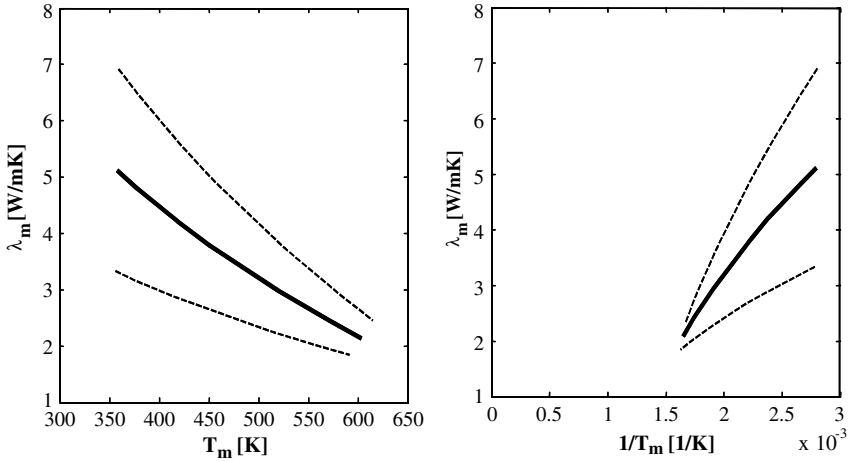

Fig. 4. Thermal conductivity of tubular inorganic membranes, made of α-Al_2O_3 (solid lines: Eq. (26), broken lines indicate maximal deviations in the data).

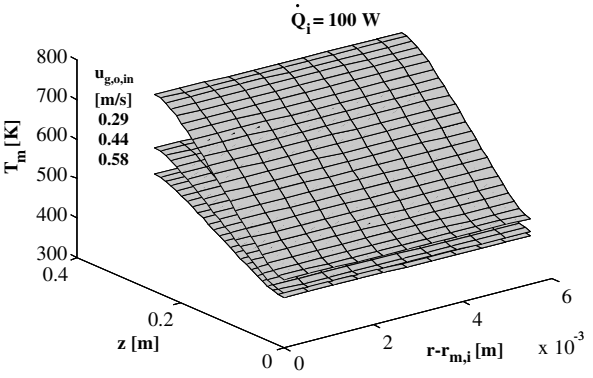

Fig. 5. Simulated, steady state, two-dimensional temperature field in the membrane for three different gas flow velocities.

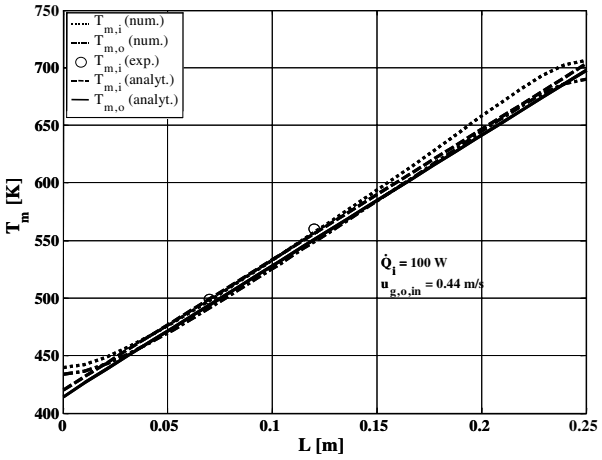

Fig. 6. Numerically and analytically calculated axial profiles of membrane temperature compared with measured values.

identification of λ_m, knowledge of the gas-side heat transfer coefficient in the annulus, $\alpha_{g,o}$, see Eq. (2d). The latter has been determined after [27] for thermally and hydrodynamically fully developed laminar flow and constant heat flux. The temperature profiles are flat at $z = 0$ and $z = L$, due to the consideration of axial conduction and the adiabatic boundary conditions of Eqs. (3), but approximately linear in the middle section of the membrane, where the temperature measurements took place (Fig. 5). Axial and radial differences and gradients correspond to the measured values, as previously indicated.

The problem solved numerically in Fig. 5 can be somewhat simplified by neglecting axial conduction and the temperature dependence of membrane thermal conductivity. Then, analytical solution is possible. Axial membrane temperature profiles calculated after this analytical solution, calculated after the numerical solution, and measured are compared in Fig. 6, with good agreement. As already stressed, the coefficient of gas-side heat transfer, $\alpha_{g,o}$, is not important for the identification of λ_m, but is important for the level of temperature at different axial positions. Results like those of Fig. 6 are the steady-state asymptotes of the transients that will be discussed in Section 6.2.

6.2. Validation experiment: transient heat transfer

In transient thermal experiments the change of membrane surface temperature is monitored after switching on the electrical heater at $t = 0$ (Fig. 1b). These experiments are modelled by numerically solving the same set of equations as for the steady-state heat transfer case, though expanded by the accumulation term at the left-hand side of Eq. (1). To this purpose the thermal diffusivity of the membrane,

$$\kappa_m = \frac{\lambda_m}{\rho_m c_m}, \tag{27a}$$

is calculated from thermal conductivities after Eq. (26), the density of $\rho_m = 2820\ \mathrm{kg/m^3}$, which has been obtained from the mass and volume of the membrane ($V_m = 0.000114\ \mathrm{m^3}$), and the specific heat capacity, c_m, which has been determined separately by differential scanning calorimetry. In contrary to the thermal conductivity, the specific heat capacity of the membrane increases slightly with increasing temperature, especially in the low temperature range. It has been correlated empirically to

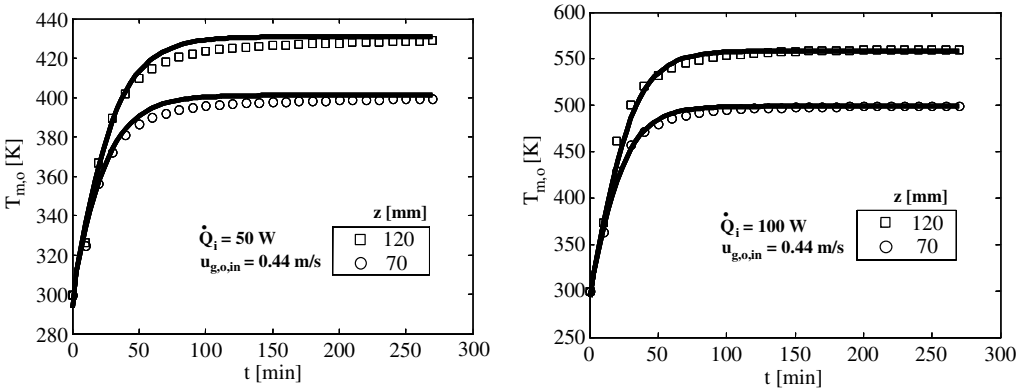

Fig. 7. Comparison between measured and predicted transients of membrane outer side temperature, at for two different axial locations and heater capacities.

$$c_m = -0.0009T_m^2 + 1.6804T_m + 388.88 \quad (27b)$$

with c_m in J/(kg K) and T_m in K.

Since nothing is fitted, the transient thermal experiments are pure validation experiments, confirming the values of membrane thermal conductivity derived in the previous section. This validation is successful, as the good agreement between measurement and prediction in Fig. 7 exemplarily shows. The respective experiments have, again, been conducted at various gas and heat flow rates. The influence of parameters like the thermal capacity of the electrical heater and the outer reactor cage, imperfect insulation of the reactor ends, and heat losses to the environment has been studied with the help of adequate, extended model versions, and found to be low in case of the transient heat transfer experiments.

7. Mass transfer experiments

Mass transfer experiments enable the identification and validation of all mass transport parameters of the membrane. Single gas permeation experiments (Fig. 1c) have been performed mainly for the identification of structural parameters of every membrane layer by using air, N_2 and He for different temperatures (20–500 °C) and pressures (1–3 bar). Isobaric diffusion experiments (Fig. 1d) and the transient diffusion experiments (Fig. 1e) have been conducted for validation of the layer transport parameters identified by single gas permeation. Hence, only the composite membrane has been used for these experiments, which have been performed with N_2 and He at room temperature.

7.1. Single gas permeation

The principle of steady state, single gas permeation measurements is depicted in Fig. 1c, see also [18–22]. As the sketch shows, the gas is introduced in the annulus, flows through the membrane due to the pressure difference ΔP, and leaves the cell at the end of the tube. In this case, and for a homogeneous membrane, the general DGM equation (11) reduces to

$$\dot{n}_j = -\frac{1}{\widetilde{R}T}\left(\frac{4}{3}K_0\sqrt{\frac{8\widetilde{R}T}{\pi\widetilde{M}_j}} + \frac{B_0}{\eta_j}\overline{P}\right)\nabla P. \quad (28)$$

For cylindrical coordinates and a relatively moderate membrane thickness the expression

$$\frac{\dot{N}_j}{\Delta P} = -\frac{2\pi L}{\widetilde{R}T\ln\left(\frac{r_{m,o}}{r_{m,i}}\right)}\left(\frac{4}{3}K_0\sqrt{\frac{8\widetilde{R}T}{\pi\widetilde{M}_j}} + \frac{B_0}{\eta_j}\overline{P}\right) \quad (29)$$

is obtained by integration of Eq. (28).

In Eq. (29), $\overline{P}$ is the mean pressure in the membrane, $\overline{P} = (P_o + P_i)/2$, ΔP is the pressure drop, $\Delta P = P_o - P_i$. In experiments with a homogeneous membrane the pressure level, i.e., $\overline{P}$, is varied, while the pressure difference, ΔP, and P_i, P_o, or both are measured. Additionally, the gas flow rate, which permeates through the membrane, is determined, and converted to the gas molar flow rate, $\dot{N}_j$. With known geometry of the membrane (L, $r_{m,o}$, $r_{m,i}$) and gas properties, the parameters of the dusty gas model, K_0 and B_0, can then be derived. Specifically, and due to the linearity of Eq. (29), the Knudsen coefficient, K_0, is derived from the intercept, and the permeability constant, B_0, from the slope of a plot of the ratio $\dot{N}_j/\Delta P$ versus the mean pressure $\overline{P}$.

If, now, a second homogeneous layer is added to the original membrane and the described series of permeation experiments repeated, then Eq. (29) can be applied to calculate the pressure at the interface between the first and the second layer of the composite. In this manner, pressures and flux are known for the second layer, so that the derivation of K_0 and B_0 can be conducted also for this layer, in exactly the previously discussed way. Recursively, the parameters of every layer of any composite membrane can be derived individually, provided that all intermediate membranes, starting from the support and ending with the final composite, are available. The results of this derivation for the investigated membrane are summarized in Table 1, where a considerable decrease in B_0 can be seen due to decreasing pore diameter from support to selective membrane layer.

Though the identification of K_0 and B_0 can be done with only one gas at one temperature, many experiments have been conducted in the present work for different gases at various temperatures. For every temperature, gas and layer a value pair of K_0 and B_0 has been derived, so that it could be controlled that K_0 and B_0 depend on the layer, but do not depend—apart from moderate scatter—from temperature or the gas used. The opposite validation is to show that by means of the average values of K_0 and B_0, as listed in Table 1 for every individual layer, all measured data can be predicted reliably, irrespectively of average pressure (between 1 and 3 bar), temperature, or the kind of gas. This type of validation will be exemplified in the following on selected results, which also enable to discuss a number of interesting influences.

This discussion is started with data for the support layer, as depicted in Figs. 8–10. Fig. 8 shows the influence of gas molar mass, $\widetilde{M}_j$, on the $\dot{N}_j/\Delta P$ over $\overline{P}$ lines. According to Eq. (29), the intercept (Knudsen contribution) should depend on $\widetilde{M}_j^{-1/2}$ and, thus, decrease with increasing $\widetilde{M}_j$ (Graham's law). While the molar mass does not explicitly appear in the slope, it does have an influence on viscous flow, via the dynamic viscosity of the gas, η_j, which is a function of, approximately, $\widetilde{M}_j^{-1/6}$ (see, e.g. [28, p. 76]). Consequently, the slope should depend on $\widetilde{M}_j^{1/6}$, and moderately increase with increasing mass of the gas molecules. Both trends are convincingly verified by the experimental data.

As to the influence of temperature, it should be proportional to $T^{-1/2}$ in the Knudsen, and very strong—propor-

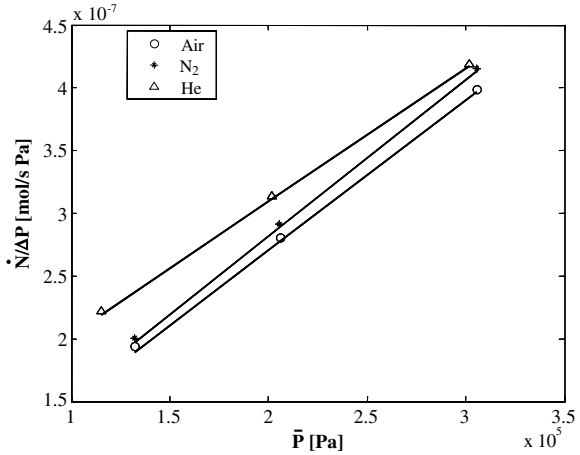

Fig. 8. Ratio of molar flow rate to pressure drop versus the average pressure for the support of the investigated membrane at 25 °C for three different gases (solid lines in this and the subsequent figures: calculations after the dusty gas model).

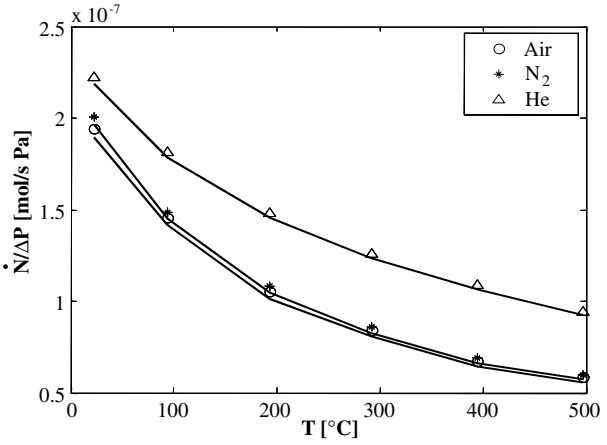

Fig. 10. Ratio of molar flow rate to pressure drop versus temperature for the support of the investigated membrane for three different gases at the lowest realised pressure level of approximately 1 bar.

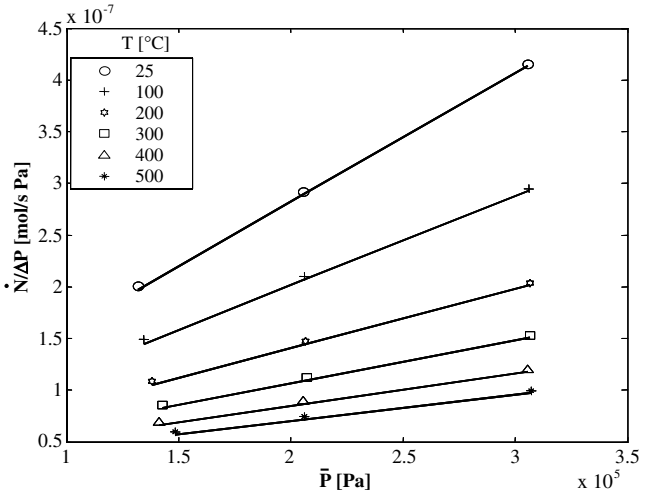

Fig. 9. Ratio of molar flow rate to pressure drop versus the average pressure for the support of the investigated membrane for N_2 at various temperatures.

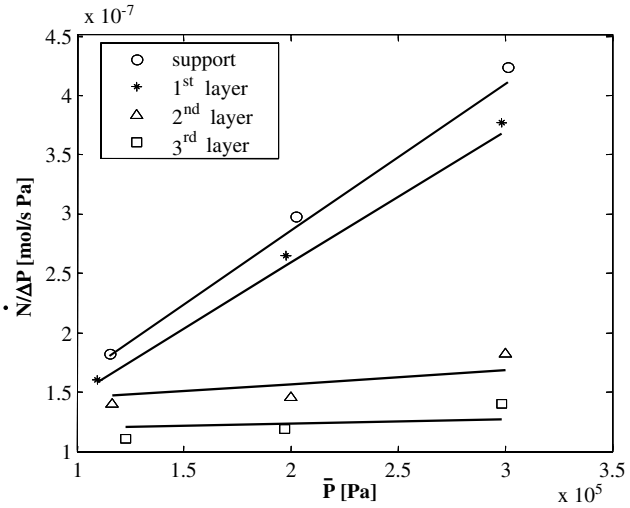

Fig. 11. Ratio of molar flow rate to pressure drop versus the average pressure for N_2 at 25 °C for every individual layer of the investigated membrane.

tional to approximately $T^{-1.75}$—in the viscous regime. Notice that the explicit, inverse proportionality on temperature of Eq. (29) and the temperature dependence of viscosity ($\eta_j \sim T^{0.75}$ [28]) go into the total influence of temperature on viscous flow. The described behaviour is verified by the intercepts and slopes of the data of Fig. 9. In the total, the temperature influence depends on the proportion between Knudsen diffusion and viscous flow, which is a matter of membrane structure and pressure level. For moderate pressures in the rather permeable support (Fig. 10), the flow rate comes out to depend approximately on $1/T$ according to the calculation and the measurements. The linearity between flow and average pressure is pointed out in both Figs. 8 and 9.

Fig. 11 shows the molar flow rates of N_2 at ambient temperature through every individual layer of the membrane, divided by the respective pressure drop and plotted against the mean pressure. It is obvious that the flow rate is strongly influenced by the mean pressure in case of the support and the first layer, as there is a large contribution of viscous flow in these membranes, due to their relatively large pore diameters. In contrary, Knudsen diffusion dominates in the second and third layer. Since Knudsen diffusion is independent of pressure, the respective lines are very flat in Fig. 11. Notice that the expression $\ln(r_{m,o}/r_{m,i})$ in Eq. (29) reduces to the ratio of layer thickness to $r_{m,i}$ for large radii of the membrane.

Results for the complete composite membrane are presented in Figs. 12 and 13. At a first glance, Fig. 12 appears to be a simple counterpart of Fig. 8. However, this impression is misleading. While Fig. 8 refers to one homogeneous layer (the support), and allows for a clear distinction between Knudsen and viscous contribution, various such contributions for different layers are combined in Fig. 12,

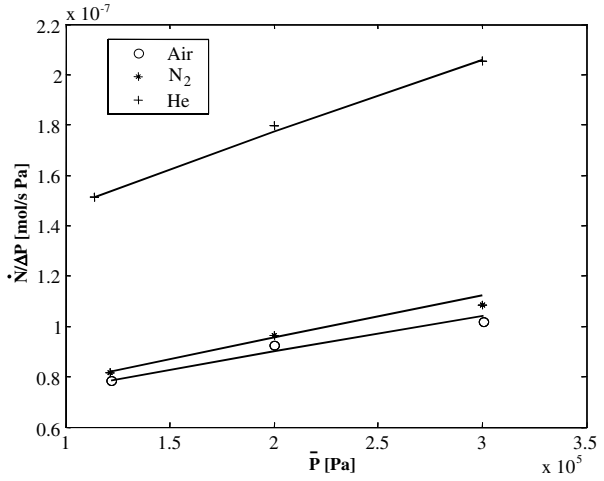

Fig. 12. Ratio of molar flow rate to pressure drop versus average pressure for the composite membrane at 25 °C for three different gases.

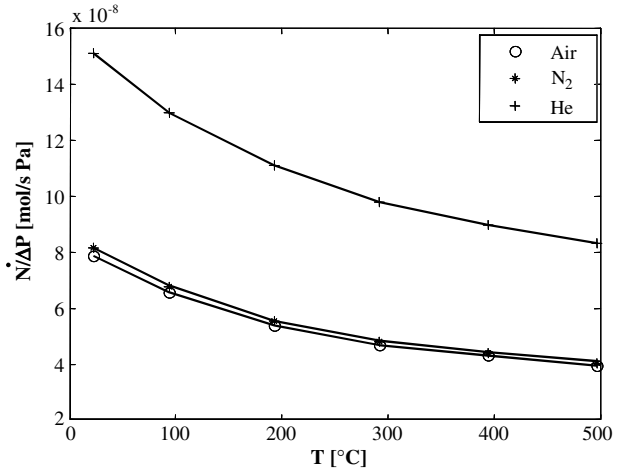

Fig. 13. Ratio of molar flow rate to pressure drop versus temperature for the composite membrane for three different gases at the lowest realised pressure level of approximately 1 bar.

with an overall enhancement of the role of Knudsen diffusion. The results are flatter curves than in Fig. 8. Another striking result is that the slope of these curves increases with decreasing molar mass of the gas in Fig. 12, while it decreases with decreasing $\widetilde{M}_j$ in Fig. 8. In other words, the composite shows in respect to a change of molar mass exactly the opposite behaviour than the support. This finding can be generalised: Indeed, the composite can behave in a different way than a homogeneous membrane, even in a different way than every of its own constituent layers. Otherwise, the behaviour of the composite and of the individual layer can also be similar, as the linearity of the curves in Fig. 12 shows. Consequently, proper consideration of asymmetry and multilayer structure is a pre-supposition for the physically consistent description of mass transport in composite membranes. As to Fig. 13, it shows that the total influence of temperature is considerably weaker in the composite membrane than in the support (Fig. 10), due to the increased role of Knudsen diffusion. The flow rates are lower for the composite, as expected.

The structural parameters d_p and ε/τ, as derived from K_0 and B_0 by means of Eqs. (24) and (25), are given in Table 1 for every membrane layer. In respect to the pore diameter, d_p, we see a coarse agreement with the nominal values according to the producer—with exception of the first and third layers, which appear to have wider pores than intended. As to the ratio ε/τ—essentially F_0 (Eq. (23))—it should be noticed that correlations exist in literature that describe this parameter as a function of porosity alone [29]. The values of ε/τ in Table 1 correspond, according to such correlations, to porosities in the range of 0.2–0.4, which is reasonable for layers consisting of small primary particles. However, such comparisons can only be indicative, for many reasons: uncertainties of identification caused by the joint influence of d_p and ε/τ on K_0 and B_0; the fact that all present derivations have been carried out with the layer thicknesses indicated by the producer, while in reality the transition from one to the other layer is not sharp; inhomogeneities and defects of the real membranes; and, finally, the unrealistic assumptions associated with Eqs. (24) and (25). Realistic transition from the microstructure of porous media to their macroscopical properties is a major, but still unsolved problem.

7.2. Validation experiment: isobaric diffusion

Additional validation of the parameters of the dusty gas model derived from single gas permeation is provided by the isobaric diffusion experiment. In this experiment, constant but different flow rates of different gases are sent through the annulus and the tube of the measuring cell at constant temperature and pressure. Gas flow rates and molar fractions are measured at the outlet (Fig. 1d).

With similar assumptions as in Section 7.1, the general equation of the dusty gas model (Eq. (11)) reduces for the present experiment to

$$\sum_{k=1,k\neq j}^{N} \frac{\tilde{x}_k\dot{n}_j - \tilde{x}_j\dot{n}_k}{\varepsilon/\tau}\frac{D_{\mathrm{K},j}}{D_{jk}} + \dot{n}_j = -\frac{P}{\widetilde{R}T}D_{\mathrm{K},j}\frac{\Delta\tilde{x}_j}{\bar{r}\ln\left(r_{\mathrm{m,o}}/r_{\mathrm{m,i}}\right)} \tag{30}$$

with $\bar{r} = (r_{\mathrm{m,o}} + r_{\mathrm{m,i}})/2$, and is applicable to every individual membrane layer.

The component mass balances in the two gas compartments are calculated by Eqs. (12) and (13), though neglecting axial dispersion in the present case [17,18]. Gas-side mass transfer coefficients have been calculated after [30] for the fully developed laminar flow.

Solution of model equations allows the determination of molar fractions and gas velocities at the outlets of the measuring cell. It has been implemented in the simulation environment ProMoT/Diva [31]. Experiments have been carried out with the composite membrane, a constant flow velocity ($u_{\mathrm{g,o,in}} = 0.06$ m/s) of pure nitrogen at the inlet of

the annulus and various flow velocities of pure helium at the inlet of the tube ($u_{g,i,in} = 0.024$–0.096 m/s). Experimental results are plotted in Figs. 14 and 15 as the helium molar fraction at the outlet of tube and annulus, $\tilde{x}_{He,i,out}$, respectively, $\tilde{x}_{He,o,out}$, and the flow velocity at the outlet of the tube, $u_{g,i,out}$, versus the flow velocity of pure helium at the inlet of the tube, $u_{g,i,in}$. With increasing value of the latter, the change of the molar fraction of helium during the flow through the cell decreases, so that $\tilde{x}_{He,i,out}$ is closer to the inlet value of $\tilde{x}_{He,i,in} = 1$ (Fig. 14). With decreasing $u_{g,i,in}$ the difference of helium molar fraction between the tube and the annulus decreases, that means equilibrium is, as expected, approached. Equilibrium (equality of molar fractions between tube and annulus) would have been approached without changes of gas flow rates in case of pure binary molecular diffusion. This is not true according to the experiments. Actually, gas flow

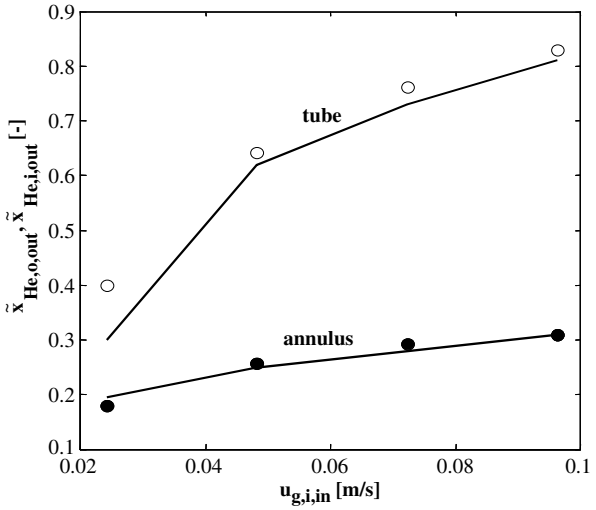

Fig. 14. Molar fraction of helium at the outlet of tube and annulus versus the flow velocity of gas (pure helium) at the inlet of tube (composite membrane, $T = 25$ °C, ambient pressure; solid lines: model predictions).

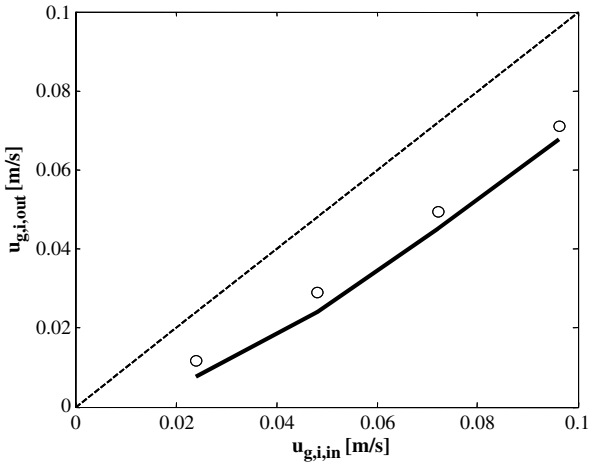

Fig. 15. Flow velocity of the gas at the outlet of the tube versus the flow velocity of gas (pure helium) at the inlet of tube.

rate decreases in respect to the inlet value in the tube (Fig. 15) and increases in the annulus (not plotted), due to preferential Knudsen diffusion of the smaller molecule (helium) through the membrane. In other words, equimolarity is abrogated because of the presence of Knudsen diffusion, and Stefan fluxes occur even in case of a binary mixture. The calculations reveal a good agreement with measured data in Figs. 14 and 15, and, since nothing has been fitted, validate additionally the previously identified mass transport parameters K_0 and F_0, or d_p and ε/τ.

7.3. Validation experiment: transient diffusion

Due to the absence of bulk flow, the steady-state isobaric diffusion experiments can validate only two structural parameters of the membrane, namely K_0 and F_0. The transient diffusion experiments validate, in contrary, all structural parameters (K_0, B_0, F_0) by implementing the whole DGM equation [17,18]. The general principle of these experiment is shown in Fig. 1e.

Transient diffusion experiments have been conducted by using N_2 and He. During the experiment, the inlet and outlet of the annulus are kept closed, so that gas flows only through the tube of the measuring cell. Before starting the measurement, only N_2 flows in the tube. Pressures on both sides of the membrane are equal and constant ($P_o = P_i$). The measurement starts at $t = 0$ by switching the flow into the tube from N_2 to He. Non-equimolar gas diffusion between both volumes of the measuring cell, annulus and tube, is the result. As the molecular weight of helium is less than that of N_2, helium will diffuse preferentially through the membrane to the annulus, increasing there the pressure to $P_o(t) > P_i$. In general, the magnitude and direction of pressure rise depend on the ratio of molecular weights of the two gases, membrane structural parameters and the gas flow rate. After reaching its maximum, the pressure in the annulus decreases again by decreasing diffusive and increasing viscous flow until the exchange process is completed ($P_o(t) \to P_i$).

To predict such pressure transients the complete DGM equation (11) is used. In absence of flow-through, spatially constant conditions can be assumed in the annulus. Consequently, and by application of the ideal gas law (Eq. (9a))

$$\frac{dP_o}{dt} = \frac{\tilde{R}TA_{m,o}}{V_o}\left(\dot{n}_{j,m,o} + \dot{n}_{k,m,o}\right) \tag{31}$$

is obtained. The mass balance of the tube is taken after Eq. (13), neglecting the dispersion term.

Experiments have been carried out with the composite membrane and its support at ambient temperature with $u_{g,i,in} = 0.03$ m/s. The comparison between experimental and simulation results is shown in Fig. 16. As expected, the composite membrane, which has layers with small pore diameters and offers more resistance to bulk flow, shows the higher pressure rise. For the support membrane the pressure rise is lower, since higher permeability facilitates equilibration by bulk flow. Prediction by the model is

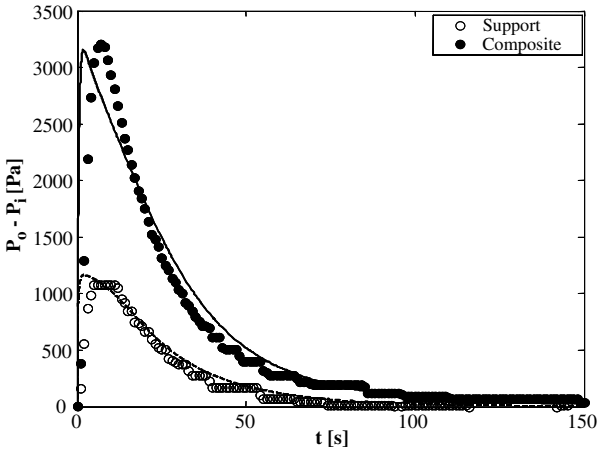

Fig. 16. Pressure rise in annulus versus time for the support and the composite membrane.

good. Experiments have also been conducted at 373 K, without significant further insight.

8. Validation experiment: coupled heat and mass transfer

Final validation of all transport parameters of the membrane is conducted by combined heat and mass transfer according to Fig. 1f. The experiment is similar to isobaric diffusion (Fig. 1d), with the important difference that now the inlet gases are at different temperatures. Not only the outlet flow rates and composition, but also the outlet temperatures of the gases are measured and calculated. The temperature of the membrane is measured on both sides by in total four miniature thermocouples, pairwise fixed at axial positions of approximately $z = 125$ and 175 mm. Again, pure nitrogen enters the annulus, and pure helium the tube. Only the composite membrane was investigated.

In the evaluation, the mass transfer equations of Section 4 are used without axial dispersion, in the same reduced form of the dusty gas model as for isobaric diffusion (Eq. (30)). Mass transfer coefficients, $\beta_{g,i}$ and $\beta_{g,o}$, in the tube and annulus are determined after [30]. Heat transfer in the membrane is treated as one-dimensional by simplifying the steady-state equation (1) in the radial direction. Heat transfer in the empty parts (annulus/tube) is considered as one-dimensional in the axial direction. Heat transfer coefficients, $\alpha_{g,i}$ and $\alpha_{g,o}$, are calculated from the respective mass transfer coefficients by application of the Lewis-analogy ($Nu/Sh = [Pr/Sc]^{1/3}$). Axial dispersion is, again, neglected by setting the first left-hand side terms of Eqs. (5) and (6) to zero. At the same time, the energy balance for the annulus (Eq. (5)) is expanded to

$$-\frac{\mathrm{d}\left(u_{g,o} n_{g,o} \tilde{c}^{av}_{p,g,o} T_{g,o}\right)}{\mathrm{d}z} + \left\{\dot{q}_{m,o} + \dot{q}_{shell,o} + \sum_j \left(\dot{n}_{j,m,o} \tilde{c}_{p,g,j} T_{m,o}\right)\right\} \frac{2\pi r_{m,o}}{F_o} = 0 \tag{32}$$

with

$$\dot{q}_{shell,o} = \alpha_{g,o}(T_{shell} - T_{g,o}). \tag{33}$$

The flux $\dot{q}_{shell,o}$ describes heat transferred from the insulated shell of the reactor to the gas flowing in the annulus. In the experiments a heater was placed close to the inlet of the tube to heat the entering gas at desired temperatures. Thermal bridges to the shell lead to somewhat increased shell temperatures, T_{shell}, which were measured by additional thermocouples and found to be almost constant along the shell at steady state. Since measured shell temperatures are inserted in Eq. (33), the correction does not involve any fitting. Its influence is noticeable for the coupled heat and mass transfer experiment, though not too large. A further consequence of space, sealing and constructive restrictions at the ends of the reactor is that the inlet gas temperature to the annulus is influenced by the operating conditions of the tube-side, so that $T_{g,o,in}$ can be measured accurately, but can not be accurately set to prescribed values.

The model equations have, again, been solved by ProMoT/Diva. A comparison with selected experimental data is presented in Figs. 17 and 18. Fig. 17 compares measured and calculated values of molar fraction at the outlet of the annulus for different inlet gas temperatures and flow velocities. It can be seen that the mole fraction of He at the outlet of the annulus rises with temperature as both diffusion coefficients, Knudsen and molecular, increase with increasing temperature. Whereas the outlet molar fraction of helium decreases with increasing volumetric flow rate, which can be justified by decreasing residence time of gas in the tube. Fig. 18 shows the comparison between measured and calculated gas temperatures at the outlet of annulus and tube. The temperature of the gas at the outlet of the annulus decreases by increasing flow velocity due, again, to less residence time of hot helium flowing through the tube (empty symbols). For the same reason, the temperature of gas at the outlet of the tube increases with increasing gas flow velocity (full symbols). Without shell correction, the trends in Fig. 18 would be stronger. It should be noticed that heat transfer takes place due to

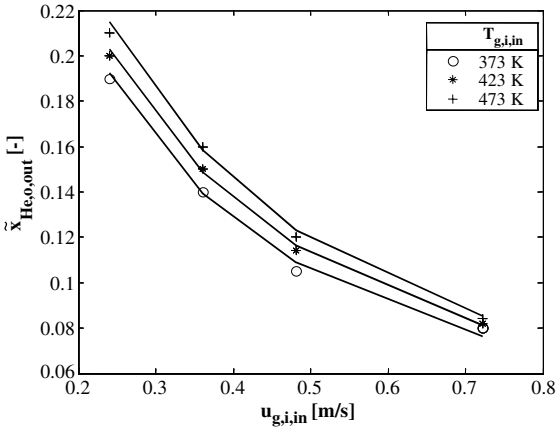

Fig. 17. Measured and predicted mole fraction of He at the outlet of annulus at different gas inlet temperatures versus inlet gas flow velocity.

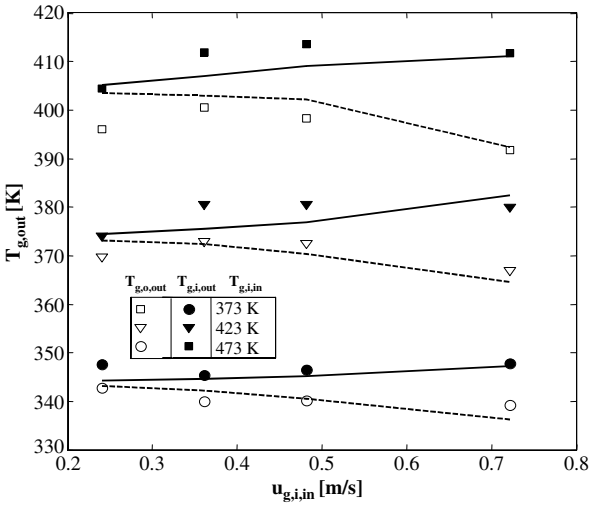

Fig. 18. Temperatures of gas at the outlet of tube and annulus at different gas inlet temperatures versus inlet gas flow velocity.

conduction along the entire length of the membrane, but in the middle part of it, which is not sealed, heat is also transferred by transmembrane enthalpy flux. In all comparisons, a reasonable agreement between measured and predicted values could be observed. This includes membrane temperatures (not depicted here).

9. Conclusion

In the present work heat and mass transfer in tubular asymmetric ceramic membranes suitable for applications in membrane reactors have been investigated. With an inner diameter of 21 mm the membranes were larger than in previous work, getting closer to industrial scale. The experimental matrix employed for steady state and dynamic measurements successfully enables the identification and validation of heat and mass transfer parameters in a comprehensive and consistent manner. Thermal conductivity of the membrane has been identified by steady state and validated in dynamic heat transfer experiments. Structural parameters of the composite membrane (mass transfer parameters) are identified by single gas permeation experiments and validated by isobaric, steady state and transient diffusion experiments. The single gas permeation experiments have been carried out not only for the composite membrane, but also for every precursor and intermediate, starting from the support. In this way, the identification of mass transfer parameters could be conducted separately for every individual layer. Doing so, the influences of temperature, pressure and molar mass of the gas can be precisely understood and accurately predicted by means of the dusty gas model, which successfully combines the mechanisms of Knudsen diffusion, viscous flow and molecular diffusion. Finally, the identified transport parameters of the membrane have been additionally validated by combined heat and mass transfer experiments.

While identification and validation of membrane transport parameters are one important aspect, the work also shows that membrane reactor configurations can be reliably modelled in the limiting case without chemical reaction. Even in this case, thermal effects and the interrelation between heat and mass transfer should be accounted for. Treatment of catalytically active membranes and packed bed membrane reactors will be the next steps of research.

Acknowledgements

The financial support of the German Research Foundation (research group "Membrane supported reaction engineering", FOR 447/1-1) is gratefully acknowledged. We thank Dr. Michael Mangold (Max-Planck Institute, Magdeburg) for helping to implement the models in ProMoT.

References

[1] J. Sanchez, T.T. Tsotsis, Catalytic Membranes and Membrane Reactors, Wiley VCH, New York, 2002.
[2] A.G. Dixon, Recent research in catalytic inorganic membrane reactors, Int. J. Chem. Reactor Eng. 1 (2003) R6.
[3] H. Weyten, K. Keizer, A. Kinoo, J. Luyten, R. Leysen, Dehydrogenation of propane using a packed-bed catalytic membrane reactor, AIChE J. 43 (7) (1997) 1819–1827.
[4] P. Quicker, V. Höllein, R. Dittmeyer, Catalytic dehydrogenation of hydrocarbons in palladium composite membrane reactors, Catal. Today 56 (1–3) (2000) 21–34.
[5] H. Weyten, J. Luyten, K. Keizer, L. Willems, R. Leysen, Membrane performance: the key issues for dehydrogenation reactions in a catalytic membrane reactor, Catal. Today 56 (1–3) (2000) 3–11.
[6] Y. Zeng, Y.S. Lin, S.L. Swartz, Perovskite-type ceramic membrane: synthesis, oxygen permeation and membrane reactor performance for oxidative coupling of methane, J. Membr. Sci. 150 (1) (1998) 87–98.
[7] H.P. Hsieh, Inorganic Membrane Separation Technology, Blackie, London, 1996.
[8] P.M. Biesheuvel, H. Verweij, Design of ceramic membrane supports: permeability, tensile strength and stress, J. Membr. Sci. 156 (1) (1999) 141–152.
[9] A.G. Dixon, W.R. Moser, Y.H. Ma, Waste reduction and recovery using O_2-permeable membrane reactors, Ind. Eng. Chem. Res. 33 (12) (1994) 3015–3024.
[10] C.-Y. Tsai, Y.H. Ma, W.R. Moser, A.G. Dixon, Modeling and simulation of a nonisothermal catalytic membrane reactor, Chem. Eng. Commun. 134 (1995) 107–132.
[11] X. Tan, K. Li, Investigation of novel membrane reactors for removal of dissolved oxygen from water, Chem. Eng. Sci. 55 (7) (2000) 1213–1224.
[12] M. Pedernera, R. Mallada, M. Menendez, J. Santamaria, Simulation of an inert membrane reactor for the synthesis of maleic anhydride, AIChE J. 46 (12) (2000) 2489–2498.
[13] M.A. Al-Juaied, D. Lafarga, A. Varma, Ethylene epoxidation in a catalytic packed-bed membrane reactor: experiments and model, Chem. Eng. Sci. 56 (2) (2001) 395–402.
[14] C. Fukuhara, A. Igarashi, Two-dimensional simulation of a membrane reactor for dehydrogenation of ethylbenzene, considering Heat and Mass Transfer, J. Chem. Eng. Jpn. 36 (5) (2003) 530–539.
[15] D.L. Meixner, P.N. Dyer, Characterization of the transport properties of microporous inorganic membranes, J. Membr. Sci. 140 (1) (1998) 81–95.
[16] U. Beuscher, C.H. Gooding, The influence of the porous support layer of composite membranes on the separation of binary gas mixtures, J. Membr. Sci. 152 (1) (1999) 99–116.
[17] A. Tuchlenski, O. Schramm, A. Seidel-Morgenstern, Steady state and dynamic mass transfer of gases in porous materials, Coll. Czech. Chem. Commun. 62 (7) (1997) 1043–1056.

[18] A. Tuchlenski, P. Uchytil, A. Seidel-Morgenstern, An experimental study of combined gas phase and surface diffusion in porous glass, J. Membr. Sci. 140 (2) (1998) 165–184.
[19] P. Capek, A. Seidel-Morgenstern, Multicomponent mass transport in porous solids and estimation of transport parameters, Appl. Catal. A: Gen. 211 (2) (2001) 227–237.
[20] P. Uchytil, O. Schramm, A. Seidel-Morgenstern, Influence of the transport direction on gas permeation in two-layer ceramic membranes, J. Membr. Sci. 170 (2) (2000) 215–224.
[21] S. Thomas, R. Schäfer, J. Caro, A. Seidel-Morgenstern, Investigation of mass transfer through inorganic membranes with several layers, Catal. Today 67 (1–3) (2001) 205–216.
[22] S. Thomas, Kontrollierte eduktzufuhr in membranreaktoren zur optimierung der ausbeute gewünschter produkte in parallel- und folgereaktionen, Ph.D. thesis, Otto-von-Guericke-Universität Magdeburg, Germany, 2003.
[23] R.C. Reid, J.M. Prausnitz, B.E. Powling, The Properties of Gases and Liquids, McGraw Hill, New York, 1987.
[24] M. Bengisu, Engineering Ceramics, Springer, Berlin, 2001.
[25] J.S. Dugdale, D.K.C. McDonald, Lattice thermal conductivity, Phys. Rev. 98 (1955) 1751–1752.
[26] A.W. Lawson, On the high temperature heat conductivity of insulators, J. Phys. Chem. Solids (1–2) (1957) 155–156.
[27] V. Gnielinski, Section Gd in VDI-Waermeatlas, sixth ed., VDI Verlag, Düsseldorf, 1991.
[28] E.U. Schlünder, E. Tsotsas, Wärmeübertragung in Festbetten, Durchmischten Schüttungen und Wirbelschichten, Thieme Verlag, Stuttgart, 1988.
[29] E. Tsotsas, Section Deb in VDI-Waermeatlas, ninth ed., Springer Verlag, Berlin, 2002.
[30] F. Lipnizki, R.W. Field, Mass transfer performance for hollow fiber modules with shell side axial feed flow: using an engineering approach to develop a framework, J. Membr. Sci. 193 (2) (2001) 195–208.
[31] M. Mangold, S. Motz, E.D. Gilles, A network theory for the structured modelling of chemical processes, Chem. Eng. Sci. 57 (19) (2002) 4099–4116.